A Design Method to Minimize Detuning for Double-Sided *LCC*-Compensated IPT System Improving Efficiency Versus Air Gap Variation

Bin Yang, *Student Member, IEEE*, Yiming Zhang, Chenyan Zhu, Subham Sahoo, *Senior Member, IEEE*, Yang Chen, *Member, IEEE*, Ruikun Mai, *Senior Member, IEEE*, Zhengyou He, *Senior Member, IEEE*, and Frede Blaabjerg, *Fellow, IEEE*

***Abstract*—Inductive power transfer (IPT) technology has garnered considerable attention due to its widespread range of applications. The variation in the air gap can result in variations in the loosely coupled transformer (LCT) parameters, including self-inductance and mutual inductance, due to positional deviations with the ferrite cores on both sides. These variable LCT parameters can damage the resonant tank, ultimately resulting in reduced efficiency. To address this problem, a double-sided *LCC*-compensated IPT system with a compact decoupled coil is proposed in this article to improve the system's efficiency with respect to the air gap variation. The key idea is to neutralize the variation in LCT parameters through the use of the self-inductance variation of the decoupled coil so that the detuning degree of the system can be suppressed. Subsequently, the analysis and parametric design process of the system are elaborated. Finally, a 1-kW experimental setup is built to verify the feasibility of the proposed method. Experimental results show that the efficiency of the system proposed in this article varies from 92.63% to 74.81%, as the air gap increases from 30 to 90 mm, wherein the primary and secondary self-inductance and mutual inductance increased by 19.3% and 135.3%, respectively. Compared with the traditional method, the maximum efficiency improvement is up to 8.16%.**

***Index Terms*—Air gap, efficiency improvement, inductive power transfer (IPT), loosely coupled transformer (LCT) parameters, tuning.**

I. Introduction

INDUCTIVE power transfer (IPT) technique, which relies on the principle of electromagnetic induction coupling, is generally acknowledged to have several advantages, such as safety, convenience, and being environmentally friendly. Therefore, this promising technology has found widespread applications in implantable medical devices [1], [2], [3], consumer electronics [4], [5], [6], underwater power supplies [7], electric vehicles [8], and other fields.

In some specific applications, such as automatic guided vehicle (AGV) [9], and so on, the displacement of the air gap is generated by some physical variations. We can take AGV as an example, usually, the AGV can have high-precision tracking capability [10]. However, when loaded with different weights, the tire pressure and spring deformation will cause air gap variations for AGV [9]. Thus, the IPT system has an inevitable air gap variation in these applications. In practice, the self-inductance and mutual inductance of the loosely coupled transformer (LCT) are sensitive to air gap [11] with the effect of the ferrite cores. As a result, changing the air gap between the primary and secondary sides can introduce variation in the LCT parameters (self-inductance and mutual inductance), which can destroy the resonant tank and decrease efficiency. Since efficiency is a critical indicator of IPT system performance, tuning the resonance of the IPT system is essential.

To maintain the resonant condition of the IPT system with different air gaps, researchers have investigated various tuning methods, which can be classified into two categories: impedance adjustment and converter control.

The impedance adjustment is a typical method used to counteract the effects of detuned circuit loops resulting from LCT parameters variation in IPT systems by employing variable impedance components, such as capacitor matrix [12] and variable capacitor or inductor [13], [14], [15], [16], [17]. In [12], a capacitor matrix is proposed to optimize the impedance. By using a multi ac switch, discrete capacitance can be obtained by selecting different permutations and combinations of capacitors to compensate for the increment of LCT parameters. However, the number of capacitors and switches required to achieve the desired tuning range and precision can increase the system size and cost. Therefore, variable capacitors or inductors can be used instead of the capacitor matrix to deal with the variable LCT parameters versus the air gap. In [13] and [14], a switched capacitor formed by a single capacitor connected to MOSFETs can be employed on the primary side to address the issue of

Manuscript received 5 July 2023; revised 11 September 2023; accepted 17 September 2023. Date of publication 25 September 2023; date of current version 6 December 2023. This work was supported in part by the National Natural Science Foundation of China under Grant 52207226 and Grant U22A20222 and in part by Sichuan Science and Technology Program under Grant 2023NSFSC0819 and Grant 2023JDRC0102. Recommended for publication by Associate Editor S. Mekhilef. *(Corresponding author: Yang Chen.)*

Bin Yang, Yiming Zhang, Chenyan Zhu, Yang Chen, Ruikun Mai, and Zhengyou He are with the School of Electrical Engineering, Southwest Jiaotong University, Chengdu 611756, China (e-mail: yb@my.swjtu.edu.cn; zym981217@my.swjtu.edu.cn; zcy@my.swjtu.edu.cn; yangchen@swjtu.edu.cn; mairk@swjtu.edu.cn; hezy@home.swjtu.edu.cn).

Subham Sahoo and Frede Blaabjerg are with the Department of Energy, Aalborg University, 9220 Aalborg East, Denmark (e-mail: sssa@energy.aau.dk; fbl@energy.aau.dk).

Color versions of one or more figures in this article are available at https://doi.org/10.1109/TPEL.2023.3318652.

Digital Object Identifier 10.1109/TPEL.2023.3318652

primary detuning. Further, Li et al. [15] proposed a double-side tuning method by adding an extra switched capacitor on the secondary side. However, those methods achieved by regulating the conduction time of MOSFETs will increase the extra switching losses. As an alternative, a variable inductor can be employed by continuously altering the dc bias through the auxiliary winding in [16] and [17]. Nevertheless, this method can encounter problems, such as core saturation, high power losses, and high harmonics [18], especially in a large self-inductance variation. As a solution, the magnetic flux controllable inductor (MFCI) is proposed to address these issues [18], [19]. However, an extra full-bridge inverter, filter, and transformer are required to form the driver of MFCI, which can present challenges regarding system size, power losses, and cost.

For the converter control, a common method is to incorporate a frequency tracking strategy in the IPT system to combat the detuning caused by variations in LCT parameters [20], [21], [22]. Aiming at minimizing the phase angle between the output voltage and current of the inverter, the operated frequency of the system can be adjusted to track the resonant point. While the frequency tracking strategy can regulate the input reactance of the IPT system, it can be challenging to simultaneously ensure the circuit loop tuning in the primary and secondary sides due to the overall LCT parameters variations. Additionally, several coordinated control schemes involving multiple converters have been proposed for multitransmitter systems [25]. This method exhibits the capability to restore resonance from a detuned state through simultaneous adjustments to the output voltage ratio of the primary-side dc–dc converters [23]. Nevertheless, it still cannot address the issue of secondary-side detuning. To adjust the resonance of the secondary side, the active control of the rectifier can be used in the IPT system to resist the LCT parameters variation [24], [25]. Based on zero-crossing detection technology, the ac equivalent reactive part of the rectifier can be controlled to neutralize the detuned part caused by the self-inductance of the secondary coil. However, an extra auxiliary coil is added to provide the required reference phase for the controller and an extra transformer is employed to eliminate primary and secondary coil interference. Further, Matsuura et al. [26] found that the secondary tuning can be achieved by an additional adjustable voltage on the secondary side. Although the extra auxiliary coil and transformer are saved, an extra controlled source and inverter are added. In order to eliminate the additional components, some parameter identification methods have been proposed in [27] and [28], but it is still necessary to predetermine some system parameters (including the value of the compensated capacitor and self-inductance), which can be challenging in situations where there is an air gap variation.

Based on the above introduction, the IPT system tuning methods for the issues of air gap variation have mainly focused on active control in the past. While these techniques have shown significant improvements in the system's performance, as evidenced by test results, they have also resulted in increased system complexity and cost. Furthermore, when the system has a large LCT parameter range, a deep modulation of the controller may cause instability and failure of regulation [29]. Therefore, it is expected that the system has the ability to resist circuit detuning versus air gap variation by employing the inherent characteristic of the IPT system.

Compensation topologies play a pivotal role in the field of IPT systems as they exert direct influence over crucial system parameters, including resonant frequency, impedance characteristics, and power transfer capability. Presently, four foundational compensation topologies are prevalent in various applications: series–series, series–parallel, parallel–series, and parallel–parallel. These topologies are favored for their inherent simplicity [30]. However, it is noteworthy that the output capacity and efficiency of these four fundamental topologies are susceptible to LCT [31]. Consequently, a series of high-order compensation topologies have been introduced to mitigate these constraints, including S-SP, *LCC*-S, S-*LCC*, double-sided *LCC*, etc. [32]. Of particular interest among these alternatives is the double-sided *LCC*-compensated topology, which amalgamates the advantages of both series and parallel compensations while offering greater flexibility in parameter design on both the primary side and the secondary side. As a result, it is garnering increasing attention in the realm of the IPT technique. Initially, the double-sided *LCC* topology exhibited promising test results upon its introduction by Li et al. [33]. To enhance system performance, many noteworthy studies have been sequentially documented [32], [34], [35], [36], [37], [38], [39], [40]. In [34], [35], and [36], the analysis of the frequency characteristics of the double-sided *LCC* topology reveals the existence of multidistinct resonant frequencies. Following this, Yao et al. [37] introduced a parameter tuning method to enhance parameter design flexibility and high-order harmonic suppression capabilities. To mitigate inverter power losses, Wang et al. investigate the correlation between compensation parameters and input phase angles. A parameter optimization design approach is subsequently presented for the double-sided *LCC* topology aimed at achieving zero-voltage switching (ZVS) operation [38]. Taking into account overall system efficiency, the compensated factors of the double-sided *LCC* topology are optimized to reduce conduction losses [39]. Moreover, Chen et al. discovered that a specialized design incorporating two compensated inductors on both the primary and secondary sides of the double-sided *LCC* topology can influence efficiency significantly without requiring adjustments to the predefined system-level parameters. Consequently, they introduced an asymmetric parameter tuning method to enhance efficiency further [40]. Building upon these findings, Chen et al. [32] additionally introduced a novel parameter configuration scheme. Within this framework, they defined two compensation factors for the primary and secondary compensation inductances to enhance overall system efficiency. While these design methodologies can enhance system performance, they are most effective when the self-inductances of the LCT remain relatively constant or exhibit minor variations. Any significant changes in coil self-inductances due to air gap variation can result in a decline in system performance attributed to nonresonance.

In order to improve the ability to resist detuning against air gap variation, this article proposes a method based on the double-sided *LCC*-compensated IPT system to address the said issues that arise from variations in the air gap. The core idea is

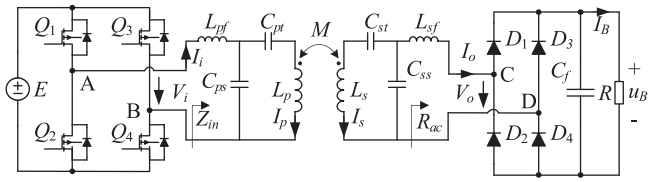

Fig. 1. Typical double-sided *LCC*-compensated topology.

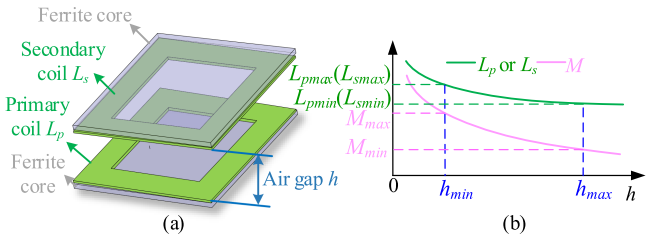

Fig. 2. (a) Typical coupling pad of the IPT system. (b) Profile of the LCT parameters versus the air gap h.

to replace the inductor on the secondary side with an integrated inductor to form a compact magnetic coupler structure. This integrated inductor changes its value with variations in the air gap to neutralize the detuned part caused by variations in LCT parameters. Additionally, the double-sided *LCC*-compensated topology circuit is simplified and analyzed based on Thevenin's theorem to, respectively, depict the overall detuning degree variation of the primary and secondary sides versus the air gap. Finally, a circuit parameter design method is proposed to suppress system detuning within a specific air gap variation range.

The rest of this article is organized as follows. In Section II, the analysis of the double-sided *LCC*-compensated topology with integrated inductance for maintaining the tuning condition is described. The parameter design procedure and an example are introduced in Section III. In Section IV, a 1-kW prototype is built to verify the theoretical analysis. Finally, Section V concludes this article.

II. Theoretical Analysis

As shown in Fig. 1, a typical double-sided *LCC*-compensated topology is given. L_{pf}, C_{ps}, C_{pt}, L_{sf}, C_{ss}, and C_{st} are the compensated inductors and capacitors of the primary and secondary sides. L_p, L_s, and M are the LCT parameters. Fig. 2(a) shows a typical LCT of IPT systems. With the utilization of the ferrite cores, the magnetic flux density increases as the secondary side approaches the primary side because the ferrite core on the secondary side serves as a small reluctance and increases LCT parameters [11]. Therefore, the profile of the LCT parameters versus air gap h can be depicted in Fig. 2(b). For simplification, L_p and L_s are considered to have the same value. $[h_{\min}, h_{\max}]$ is the predetermined range of air gap h, and the corresponding variation range of the LCT parameters are defined as $[L_{p\min}(L_{s\min}), L_{p\max}(L_{s\max})]$, and $[M_{\min}, M_{\max}]$, respectively. Then, L_p, L_s, and M can be expressed as follows according to [9]:

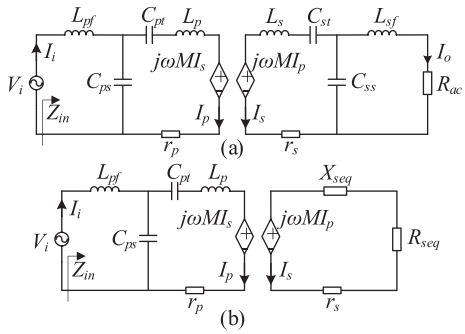

Fig. 3. Equivalent circuit of the double-sided *LCC*-compensated topology. (a) Controlled source equivalent circuit. (b) Simplified circuit of the secondary side.

$$\begin{cases} L_p = L_s = L_p(h) = L_s(h) \\ M = M(h). \end{cases} \tag{1}$$

The angular frequency of the system is $\omega = 2\pi f$, where f represents the switching frequency of the inverter. Z_{in} is the input of the system. E, V_i, u_R, and V_o are the input and output voltage of the inverter and rectifier, respectively. They can be expressed as follows [41]:

$$E = \pi \dot{V}_i / 2\sqrt{2},\ u_R = \pi \dot{V}_s / 2\sqrt{2}. \tag{2}$$

R_{ac} is the equivalent ac load. The relationship between R_{ac} and the dc load R can be given by [42]

$$R_{\text{ac}} = 8R/\pi^2. \tag{3}$$

A. Equivalent Reactance Analysis of the Secondary Side for Double-Sided LCC-Compensated Topology

According to Thevenin's theorem, the double-sided *LCC*-compensated topology circuit shown in Fig. 3(a) can be simplified as Fig. 3(b), where r_p and r_s are set as the internal resistance of the LCT. Then, X_{seq} and R_{seq} can be used to, respectively, denote the overall equivalent reactance and load part of the secondary side, which can be expressed as

$$\begin{cases} X_{\text{seq}} = -\frac{\omega C_{ss}\left(R_{\text{ac}}^2+\omega^2 L_{sf}^2\right)-\omega L_{sf}}{\omega^2 C_{ss}^2\left(R_{\text{ac}}^2+(\omega L_{sf}-1/\omega C_{ss})^2\right)} + \omega L_s - \frac{1}{\omega C_{st}} \\ R_{\text{seq}} = \frac{R_{\text{ac}}}{\omega^2 C_{ss}^2\left(R_{\text{ac}}^2+(\omega L_{sf}-1/\omega C_{ss})^2\right)}. \end{cases} \tag{4}$$

A variable α_s is used to defined to express the detuning degree of the secondary side, as

$$\alpha_s = X_{\text{seq}}/R_{\text{seq}}. \tag{5}$$

Based on Kirchhoff's voltage law, the circuit shown in Fig. 3(b) can be described as

$$\begin{cases} V_i = (j\omega L_{pf} + 1/j\omega C_{ps})\, I_i - 1/j\omega C_{ps} I_p \\ 0 = -\frac{1}{j\omega C_{ps}} I_i + \left(j\omega L_p + \frac{1}{j\omega C_{pt}} + \frac{1}{j\omega C_{ps}} + r_p\right) I_p + j\omega M I_s \\ 0 = j\omega M I_p + (jX_{\text{seq}} + R_{\text{seq}} + r_s)\, I_s. \end{cases} \tag{6}$$

When r_s is ignored, by substituting (5) into (6), the phase angle ϕ between the primary current I_p and secondary current

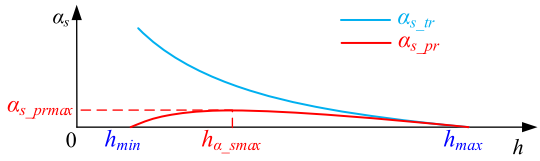

Fig. 4. α_s variation trend of the traditional method and proposed method with the different air gap h.

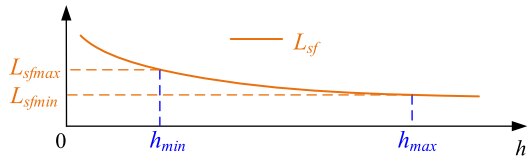

Fig. 5. Profile of L_{sf} versus the air gap h.

I_s satisfies as

$$\tan(\phi - 90^\circ) = \alpha_s = X_{\text{seq}}/R_{\text{seq}}. \tag{7}$$

Besides, the ac–ac efficiency η_{ac} of the system can be derived by solving the following equation:

$$\eta_{\text{ac}} = \frac{I_s^2 R_{\text{seq}}}{V_i \text{Re}(I_i)} = \frac{\omega^2 M^2 R_{\text{seq}}}{r_p (r_s + R_{\text{seq}})^2 + r_p \alpha_s^2 R_{\text{seq}}^2 + (r_s + R_{\text{seq}})\omega^2 M^2} \tag{8}$$

where Re($*$) represents the real component.

From (8), the efficiency η_{ac} is affected by the detuning degree of the secondary side. As α_s increases, the efficiency declines. In order to improve the efficiency, thus, α_s is always expected to be closer to zero, namely, the secondary side is resonant.

For the traditional design method of the double-sided *LCC*-compensated topology [40], the compensated components L_{pf}, C_{ps}, C_{pt}, L_{sf}, C_{ss}, and C_{st} are usually considered as the fixed value, and their relationship satisfies as

$$\begin{cases} j\omega L_{pf} + 1/j\omega C_{ps} = 0 \\ j\omega L_{sf} + 1/j\omega C_{ss} = 0. \end{cases} \tag{9}$$

Substituting (1) and (9) into (4) and (7), the phase angle ϕ_{s_tr} and detuning degree α_{s_tr} of the secondary side for the traditional method can be simplified as

$$\tan(\phi_{s\_tr}(h) - 90^\circ) = \alpha_{s\_tr}(h) = \omega C_{ss} R_{\text{ac}} \left(\omega^2 C_{ss} L_s(h) - C_{ss}/C_{st} - 1\right). \tag{10}$$

From (10), the resonance condition of the secondary side is hard to be maintained. Further, the corresponding detuning degree α_{s_tr} can be roughly drawn in Fig. 4. In order to retard the detuning, an integrated inductor formed by the decoupled coil can be used instead of the secondary compensated inductor L_{sf}.

B. Secondary-Side Tuning Method Versus Air Gap Variation

Similarly, the value of L_{sf} is also varied versus air gap with the impact of ferrite cores, which can be written as (11). And the profile of L_{sf} is depicted in Fig. 5. When the air gap h operates in a predetermined region $[h_{\min}, h_{\max}]$, the variation range of L_{sf} can also be defined as $[L_{sf\min}, L_{sf\max}]$. With the simultaneous variation of L_{sf} and L_s, the detuning degree α_s will no longer be monotonic, and the plasticity of α_s can be enhanced according to (4) and (7)

$$L_{sf} = L_{sf}(h). \tag{11}$$

Substituting (1), (4), and (11) into (7), the phase angle ϕ_{s_pr} and detuning degree α_{s_pr} of the secondary side for the proposed method can be obtained as

$$\tan(\phi_{s\_pr}(h) - 90^\circ) = \alpha_{s\_pr}(h) = \frac{L_{sf}(h) - C_{ss}\left(R_{\text{ac}}^2 + \omega^2 L_{sf}(h)^2\right)}{R_{\text{ac}}/\omega} + \frac{\left(R_{\text{ac}}^2 + (\omega L_{sf}(h) - 1/\omega C_{ss})^2\right)}{R_{\text{ac}}/\omega^2 C_{ss}^2 (\omega L_s(h) - 1/\omega C_{st})}. \tag{12}$$

Referring to [43], the relationship between L_p, L_s, and L_{sf} is fitted as (13). It is noted that there are many fitted function types. The difference between the different fitted function types mainly lies in the complexity of the calculation

$$L_p(h) = L_s(h) = aL_{sf}(h) + b \tag{13}$$

where a and b are the fitted coefficient between L_p, L_s, and L_{sf}.

To describe the variation trend, the derivate of α_s with respect to h by substituting (12) into (13) can be given by

$$\frac{d}{dh}\alpha_{s\_pr}(h) = \left(\frac{d}{dL_{sf}(h)}\alpha_{s\_pr}(h)\right)\left(\frac{d}{dh}L_{sf}(h)\right) = \left(\frac{d}{dh}L_{sf}(h)\right)\frac{\omega\left(AL_{sf}(h)^2 + BL_{sf}(h) + C\right)}{C_{st}R_{\text{ac}}} \tag{14}$$

where

$$\begin{cases} A = 3a\omega^4 C_{ss}^2 C_{st} \\ B = 2\omega^2\left(C_{ss}^2\left(b\omega^2 C_{st} - 1\right) - C_{ss}C_{st}(2a+1)\right) \\ C = \omega^2 C_{ss}C_{st}\left(aC_{ss}R_{\text{ac}}^2 - 2b\right) + aC_{st} + C_{st} + 2C_{ss}. \end{cases} \tag{15}$$

Since the values of M, L_p, L_s, and L_{sf} decrease with the rise of air gap h, the derivates of LCT parameters should satisfy $d(M)/dh < 0$, $d(L_p)/dh < 0$, $d(L_s)/dh < 0$, and $d(L_{sf})/dh < 0$ according to [9]. Thus, letting (14) equal to zero, namely, $d\alpha_{s\_pr}(h)/dh = 0$, we can obtain

$$L_{sf}(h_{\alpha\_s\max}) = \left(-B \pm \sqrt{B^2 - 4AC}\right)/2A \tag{16}$$

where $h_{\alpha\_\max}$ is the air gap corresponding to the extremal detuning degree $\alpha_{s\_pr\max}$.

Substituting (12) into (16), the maximum detuning degree $\alpha_{s\_\max}$ can be calculated as

$$\alpha_{s\_pr\max} = \alpha_{s\_pr}(h_{\alpha\_s\max}). \tag{17}$$

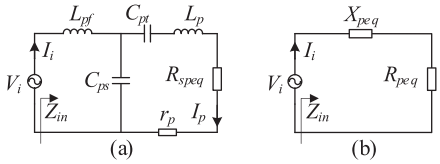

Fig. 6. Equivalent circuit of double-sided *LCC*-compensated topology. (a) Simplified circuit with the primary equivalent load reflects from the secondary side to the primary side. (b) Simplified circuit of the primary side.

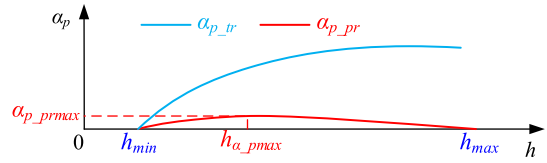

Fig. 7. α_p variation trend of the traditional method and proposed method with the different air gap h.

The profile of the detuning degree α_s of the proposed method also can be drawn by combining (14), (16), and (17), as depicted in Fig. 4. The variation trend of α_s or ϕ nonmonotonic with air gap for the proposed method. When the C_{ss} and C_{st} can be reasonably designed, the nonmonotonic region of α_s can be utilized to maintain the secondary tuning.

C. Equivalent Reactance Analysis of the Primary Side for Double-Sided LCC-Compensated Topology

For the simplified analysis, the secondary equivalent reactance X_{seq} and the internal resistance r_p and r_s of the LCT are ignored. Furthermore, the circuit in Fig. 3 is further equivalenced in Fig. 6, where R_{speq} is the equivalent load reflecting from the secondary side to the primary side, and R_{speq} can be given by

$$R_{speq} = \omega^2 M^2 / R_{\text{seq}}. \tag{18}$$

Then, the primary equivalent reactance and load part is expressed by X_{peq} and R_{peq}, which can be written as

$$\begin{cases} X_{peq} = \frac{\omega^2 L_{pf} C_{ps} - 1}{\omega C_{ps}} - \frac{D}{\omega^2 C_{ps}^2 \left(D^2 + R_{speq}^2\right)} \\ R_{peq} = \frac{C_{pt}^2 R_{speq}}{\omega^2 C_{ps}^2 \left(D^2 + R_{speq}^2\right)} \end{cases} \tag{19}$$

where $D = \omega L_p - 1/\omega C_{pt} - 1/\omega C_{ps}$.

The transfer power P_o can be obtained as

$$P_o = \left| \frac{V_i}{R_{peq} + jX_{peq}} \right|^2 R_{peq}. \tag{20}$$

Similarly, a variable α_p is employed to show the detuning degree of the primary side, which can be expressed as

$$\alpha_p = X_{peq} / R_{peq}. \tag{21}$$

And the input impedance angle θ of the system is written as

$$\tan(\theta) = \alpha_p = X_{peq} / R_{peq}. \tag{22}$$

Substituting (1) and (9) into (19) and (22), the detuning degree α_{p_tr} and input impedance angle θ_{p_tr} of the primary side for the traditional design method can be yielded as

$$\begin{aligned} \tan\left(\theta_{p\_tr}(h)\right) &= \alpha_{p\_tr}(h) \\ &= -\frac{D(h) R_{\text{ac}}}{\omega^4 M^2 C_{ss}^2 \left(R_{\text{ac}}^2 + \left(\omega L_{sf} - 1/\omega C_{ss}\right)^2\right)} \end{aligned} \tag{23}$$

where $D(h) = \omega L_p(h) - 1/\omega C_{pt} - 1/\omega C_{ps}$.

Considering the implementation of the ZVS for the inverter, the input impedance usually is resistor–inductance, namely, $\theta_{p\_tr} > 0$. Thus, we have

$$D(h) < 0. \tag{24}$$

Combining (24), the derivate of α_{p_tr} can be given as

$$\frac{d}{dh}\alpha_{p\_tr}(h) = \frac{2D(h)\frac{d}{dh}M(h) - \omega M \frac{d}{dh}L_p(h)}{\omega^2 M^3 / R_{\text{seq}}} > 0. \tag{25}$$

From (25), the detuning degree α_{p_tr} and input impedance angle θ are increased with the air gap h, and the corresponding profile can be painted in Fig. 7. As it is well-known, a slight inductance is more beneficial for reducing the switching losses of the inverter [44]. Therefore, the traditional method is hard to ensure a slight inductance due to the monotonic characteristic of α_{p_tr} when the LCT has a significant air gap variation, which is not desirable for the inverter.

D. Primary-Side Tuning Method Versus Air Gap Variation

To suppress the detuning of the primary side, the resonant relationship between L_{pf} and C_{ps} is abandoned. With the application of the integrated coil L_{sf}, the plasticity of α_p can be further improved.

Similarly, the relationship between M and L_{sf} can also be given by

$$M(h) = cL_{sf}(h)^2 + dL_{sf}(h) + e \tag{26}$$

where c, d, and e are the fitted coefficient between M and L_{sf}.

Substituting (1), (11), and (26) into (19) and (22), the detuning degree α_{s_pr} of the primary side and input impedance angle θ_{p_pr} for the proposed method can be given by

$$\begin{aligned} \tan\left(\theta_{p\_pr}(h)\right) = \alpha_{p\_pr}(h) = &-\frac{D(h)}{C_{pt}^2 R_{speq}(h)} \\ &+ \frac{\omega^2 L_{pf} C_{ps} - 1}{\omega C_{ps}} \frac{\omega^2 C_{ps}^2 \left(D(h)^2 + R_{speq}(h)^2\right)}{C_{pt}^2 R_{speq}(h)} \end{aligned} \tag{27}$$

where

$$\begin{cases} D(h) = \omega\left(aL_{sf}(h) + b\right) - 1/\omega C_{pt} - 1/\omega C_{ps} \\ R_{speq}(h) = \frac{\omega^4 (cL_{sf}(h) + d)^2 C_{ss}^2 \left(R_{\text{ac}}^2 + (\omega L_{sf}(h) - 1/\omega C_{ss})^2\right)}{R_{\text{ac}}}. \end{cases} \tag{28}$$

We can use $h_{\alpha\_p\max}$ to represent the air gap corresponding to the extremal detuning degree $\alpha_{p\_pr\max}$. Then, letting the derivate of α_{p_pr} to equal to zero, i.e., $d\alpha_{p\_pr}/dh = 0$, the

inductance value $L_{sf}(h_{\alpha\_p\max})$ of integrated coil corresponding to the extremal detuning degree $\alpha_{p\_pr\max}$ can be solved, as follows:

$$\frac{d}{dh}\alpha_{p\_pr}(h)=\frac{d\alpha_{p\_pr}(h)}{dL_{sf}(h)}\frac{dL_{sf}(h)}{dh}=0\overset{\text{solve},L_{sf}}{\rightarrow}L_{sf}(h_{\alpha\_p\max}). \tag{29}$$

Further, substituting the calculation results of (27) into (29), $\alpha_{p\_pr\max}$ and the extremal input impedance angle $\theta_{\max}$ can be given by

$$\begin{aligned}\tan(\theta_{\max})=\alpha_{p\_pr\max}=&-\frac{D(h_{\alpha\_p\max})}{C_{pt}^2R_{sp\text{eq}}(h_{\alpha\_p\max})}\\&+\frac{\omega^2L_{pf}C_{ps}-1}{\omega C_{ps}}\\&\frac{\omega^2C_{ps}^2\left(D(h_{\alpha\_p\max})^2+R_{sp\text{eq}}(h_{\alpha\_p\max})^2\right)}{C_{pt}^2R_{sp\text{eq}}(h_{\alpha\_p\max})}.\end{aligned} \tag{30}$$

By combining (29) and (30), the variation trend of detuning degree α_p and input impedance angle θ are similar with α_s. If L_{pf}, C_{ps}, and C_{pt} are rationally designed, it is also possible to create a nonmonotonic region, as shown in Fig. 7, to suppress the detuning of the primary side.

III. Design and Example

A. Constraints and Design

In order to optimize the detuning degree α_{s_pr} and α_{p_pr} of the secondary and primary sides with respect to air gap h, some constraints are necessary to assist the system design. In practice, we usually hope α_{s_pr} and α_{p_pr} are as close to zero as possible. Therefore, we can set the detuning degree to be zero when $h = h_{\min}$ ($L_p = L_s = L_{p\max} = L_{s\max}$, $M = M_{\max}$, and $L_{sf} = L_{sf\max}$), which is the first constraint, as follows:

$$\begin{cases}\alpha_{s\_pr}(h_{\min})=0\\ \alpha_{p\_pr}(h_{\min})=0.\end{cases} \tag{31}$$

Besides, when $h = h_{\min}$, the corresponding transfer power can be designed as the desired transfer power P_{od}. Then, the second constraint can be given as

$$\begin{aligned}P_{\text{od}}=&\frac{V_i^2}{R_{p\text{eq}}(h_{\min})}=\frac{V_i^2R_{\text{seq}}(h_{\min})}{\omega^2M_{\max}^2}\\=&\frac{V_i^2R_{ac}}{\omega^2M_{\max}^2\omega^2C_{ss}^2\left(R_{\text{ac}}^2+(\omega L_{sf\max}-1/\omega C_{ss})^2\right)}\end{aligned} \tag{32}$$

where $R_{p\text{eq}}(h_{\min})$ and $X_{p\text{eq}}(h_{\min})$ are the primary equivalent reactance and load part when $L_p = L_s = L_{p\max} = L_{s\max}$, $M = M_{\max}$, and $L_{sf} = L_{sf\max}$.

Furthermore, the allowable variation region for α_{s_pr} and α_{p_pr} can be defined as [0, $\alpha_{s\max}$] and [0, $\alpha_{p\max}$], when the air gap h operates within [$h_{\min}$, $h_{\max}$]. Here, $\alpha_{s\max}$ and $\alpha_{p\max}$ represent the maximum allowable detuning degree for the secondary and primary sides of the system. Then, we can establish the third constraint, i.e.,

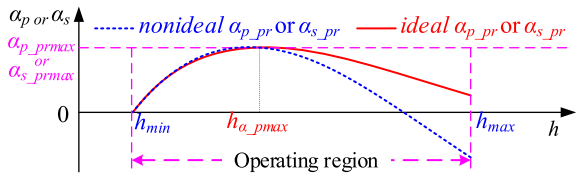

Fig. 8. Profile of α_{s_pr} and α_{p_pr} satisfying the constraints.

$$\begin{cases}\alpha_{s\_pr\max}\le\alpha_{s\max}\\ \alpha_{p\_pr\max}\le\alpha_{p\max}.\end{cases} \tag{33}$$

Based on the given constraints, the profile of α_{s_pr} and α_{p_pr} can be roughly sketched in Fig. 8. It can be seen that the detuning degree α_{s_pr} and α_{p_pr} can be located within the desired range [0, $\alpha_{s\max}$] and [0, $\alpha_{p\max}$] with the combined effect of the first and third constraints. However, there is an uncontrollable situation that occurs when $h = h_{\max}$, which can cause α_{s_pr} and α_{p_pr} to break away from the allowable limits. In order to avoid the above issues, the integrated inductor L_{sf} can be redesigned to adjust the fitting coefficients of formulas shown in (13) and (26). Hence, a common design method is given below.

First, we can predetermine the maximum secondary detuning degree $\alpha_{s\max}$ or the maximum phase angle $\phi_{\max}$ between I_p and I_s, the maximum primary detuning degree $\alpha_{p\max}$ or the maximum impedance input $\theta_{\max}$, the load R, the operated frequency f, the desired transfer power P_{od}, the variation range of the air gap [$h_{\min}$, $h_{\max}$], and the size and structure of LCT and integrated inductor L_{sf}. Then, the turn of the integrated inductor L_{sf} is initialized and the maximum turn is set as $N_{sf\max}$. Next, we can obtain the self-inductance and mutual inductance of the LCT and integrated inductor L_{sf} by Maxwell to fit the functions with the air gap h or the inductance L_{sf}. Further, the compensated components L_{pf}, C_{ps}, C_{pt}, C_{ss}, and C_{st} can be solved by substituting the fitted functions, $\alpha_{s\max}$ or $\phi_{\max}$, $\alpha_{p\max}$ or $\theta_{\max}$, R, P_{od}, f, [$h_{\min}$, $h_{\max}$] into (12), (17), (27), (30), (31), (32), and (33). Finally, substituting the calculated results and the value of the maximum air gap $h_{\max}$ into (12) and (27), the α_{s_pr} and α_{p_pr} corresponding to $h_{\max}$ can be evaluated to determine whether they locate in the required region [0, $\alpha_{s\max}$] and [0, $\alpha_{p\max}$]. If yes, L_{pf}, C_{ps}, C_{pt}, C_{ss}, and C_{st} and integrated inductor L_{sf} will be recorded. Otherwise, the turn, size, and structure will be regulated to repeat the above procedures. The flow chart is depicted in Fig. 9 to further explain the design procedure.

B. Design Example

In the previous article, decoupled coil structures have been proposed in [45] and [46], and are widely used in IPT systems to achieve magnetic integration [47], [48]. The integrated inductor formed by decoupled coils can reduce the volume without affecting the electrical performance of the system [48]. For example, a quadruple D quadrate pad is adopted in this article to form a compact magnetic coupler with integrated inductor L_{sf}, as shown in Fig. 10. Here, the primary coil L_p and secondary coil L_s act as the traditional quadrate pads (QP), while the integrated inductor L_{sf} is a quadruple D pad (QDP). The current in the

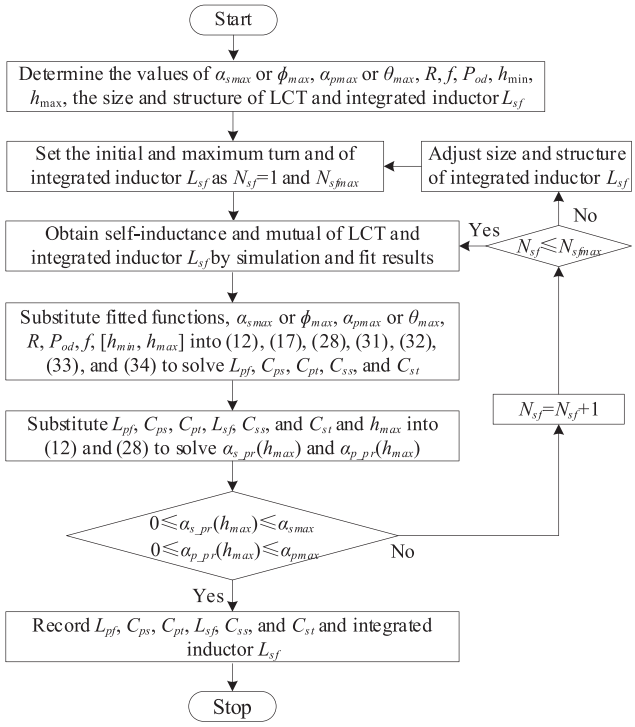

Fig. 9. Design flow chart.

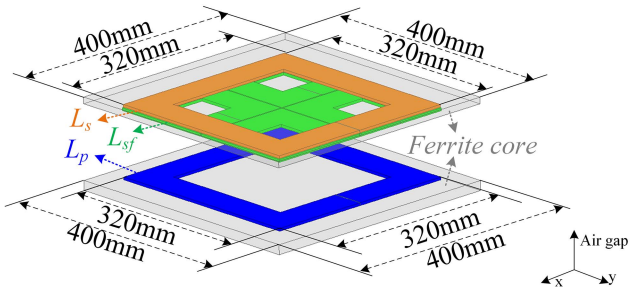

Fig. 10. Compact magnetic coupler with integrated inductor L_{sf}.

TABLE I
PARAMETERS VALUE OF PROPOSED METHOD

Parameter	Design value	Parameter	Design value
α_{smax} or ϕ_{max}	3.49% or 92°	α_{pmax} or θ_{max}	36.4% or 20°
R	40 Ω	f	90 kHz
P_{od}	1 kW	h_{min}	30 mm
h_{max}	90 mm	L_{pf}	8.47 μH
C_{ps}	89.92 nF	C_{pt}	22.22 nF
C_{st}	13.00 nF	C_{ss}	17.10 nF
L_{sf}	127.14–144.52 μH	M	40.8–95.99 μH
L_p	130.35–155.00 μH	L_s	131.17–156.16 μH
L_F	50.46 μH	C_F	62.02 nF
R_{Lpf}	17.11 mΩ	R_{Cps}	33.01 mΩ
R_{Cpt}	32.50 mΩ	R_{Cst}	242.00 mΩ
R_{Css}	11.30 mΩ	R_{Lsf}	129.4 mΩ
R_{Lp}	168.24 mΩ	R_{Ls}	145.3 mΩ
R_{LF}	33.06 mΩ	R_{CF}	11.94 mΩ

where R_{CF}, R_{LF}, R_{Lpf}, R_{Cps}, R_{Cpt}, R_{Lp}, R_{Cst}, R_{Ls}, R_{Css}, and R_{Lsf} are respectively internal resistance of components C_F, L_F, L_{pf}, C_{ps}, C_{pt}, L_p, C_{st}, L_s, C_{ss} and L_{sf}.

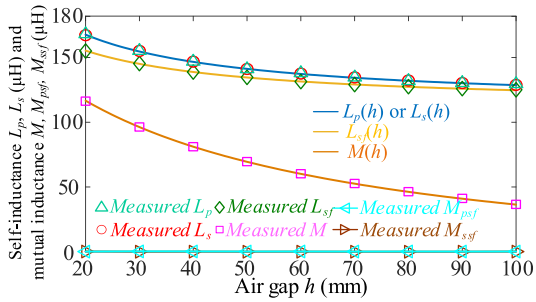

Fig. 11. LCT parameters and integrated inductor L_{sf} versus the air gap h.

TABLE II
PARAMETERS VALUE OF TRADITIONAL METHOD

Parameter	Design value	Parameter	Design value
L_{pf}	13.6 μH	C_{ps}	230.00 nF
C_{pt}	21.81 nF	C_{st}	244.31 nF
C_{ss}	21.69 nF	L_{sf}	144.52 μH
R_{Lpf}	36.45 mΩ	R_{Cps}	52.23 mΩ
R_{Cpt}	40.50 mΩ	R_{Cst}	7.07 mΩ
R_{Css}	16.32 mΩ	R_{Lsf}	198.77 mΩ

adjacent coils of the QDP should be in opposite directions to create orthogonal magnetic flux with the QP [46]. Due to the symmetry, the magnetic flux passing from the QDP (QP) to the QP (QDP) is zero in ideal conditions. Therefore, the LCT and integrated inductor L_{sf} can be decoupled, meaning that the cross-coupling between L_{sf}, L_p, and L_s, represented by M_{psf} and M_{ssf}, can be ignored. The size of the ferrite core and the coils are defined as 400 mm × 400 mm and 320 mm × 320 mm, respectively. The predetermined parameters are given in Table I. The self-inductances and mutual inductance of the LCT and integrated inductor L_{sf} have been recorded in Fig. 11, and fitting results are given in (34) and Fig. 11 as a comparison with the measured data. As a result, the values of compensated components L_{pf}, C_{ps}, C_{pt}, C_{ss}, and C_{st} are also given in Table I.

In order to show the effectiveness of the proposed method, a set of parameters of the traditional method with standalone inductor L_{sf} can be designed in Table II according to [40]. Considering the fairness of comparison, the traditional method was set to a resonant state with the value of L_{sf} selected to match that of the proposed method with the integrated inductor L_{sf} at the minimum air gap $h_{\min}$ [48]. By substituting from the parameters of Tables I and II into (12) and (30), the secondary detuning degree α_s, phase angle $\phi_{\max}$ between I_p and I_s, primary detuning degree α_p, and input impedance angle θ can be calculated and graphically displayed as Fig. 12. The graph shows that the secondary detuning degree α_{s_pr}, the phase angle ϕ_{s_pr} between I_p and I_s, the primary detuning degree α_{p_pr}, and the input impedance angle θ_{p_pr} of the proposed method consistently follow the nonmonotonic trend, as predicted by theoretical analysis. For air gaps varying from 30 to 90 mm, the values of α_{s_pr}, ϕ_{s_pr}, α_{p_pr}, and θ_{p_pr} are, respectively, located in the required ranges of [0, 3.49%], [90°, 92°], [0, 36.4%], and [0°, 20°]. In contrast, for the traditional method, α_{s_tr}, ϕ_{p_pr} α_{p_tr}, and θ_{p_tr} monotonically change as the air gap varies, with ranges of [0, −8.2%], [90°, 85.31°], [0, 516%], and [0°, 79°],

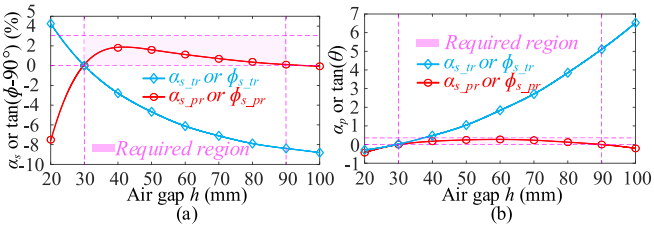

Fig. 12. Profile of (a) secondary detuning degree α_s, the phase angle ϕ between I_p and I_s, (b) the primary detuning degree α_p, and the input impedance angle θ with the different air gap.

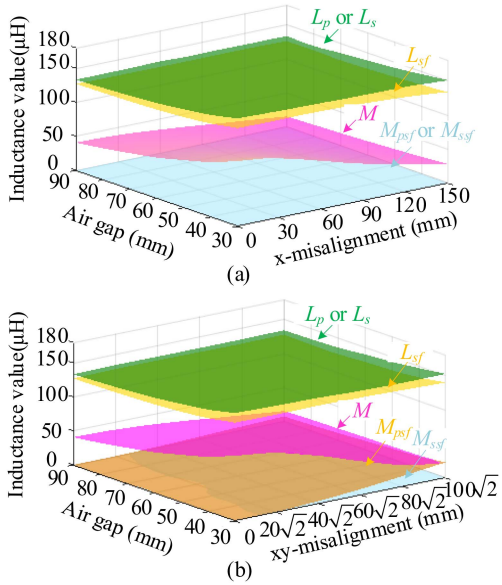

Fig. 13. LCT parameters and integrated inductor L_{sf} for the cases of (a) x-misalignment and (b) xy-misalignment.

respectively, which can be found to be significantly inferior to the proposed method. Therefore, in terms of detuning degree, the results show that the proposed method is feasible

$$\begin{cases} L_p = L_s = L_p(h) = L_s(h) = \frac{113.1h+3100}{h+11.98} \\ = 1.274L_{sf}(h) - 30.23 \end{cases}$$

$$\begin{cases} M = M(h) = \frac{-21.71h+7193}{h+37.93} \\ = -0.06641L_{sf}(h)^2 + 21.32L_{sf}(h) - 1594. \end{cases} \tag{34}$$

Furthermore, the coils parameters (self-inductances and mutual inductances between different coils) can be shown in Fig. 13 for the different direction misalignment when the air gap varies from 30 to 90 mm, where L_p, L_s, and L_{sf} are the self-inductances, M is the mutual inductance between coils L_p and L_s, and M_{psf} and M_{ssf} are the cross-coupling between L_{sf}, L_p, and L_s. When there is the x-misalignment and air gap misalignment, the self-inductances L_p, L_s, and L_{sf} and mutual inductance M of the two LCTs have large variations, while the cross-coupling M_{psf} and M_{ssf} of the compact magnetic coupler used in this article can be ignored. When there is the xy-misalignment and air gap misalignment, the variation trends of L_p, L_s, L_{sf}, M, and M_{ssf} of

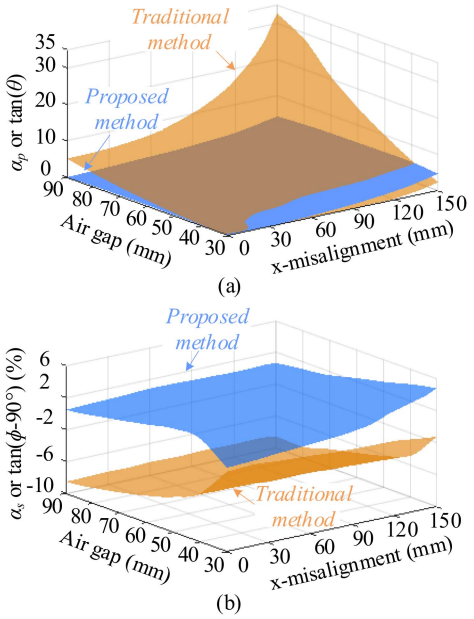

Fig. 14. Results of (a) primary detuning degree α_p, and (b) secondary detuning degree α_s versus x-misalignment.

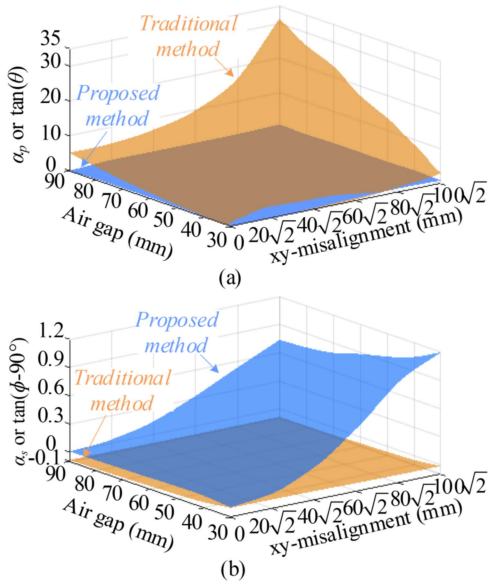

Fig. 15. Results of (a) primary detuning degree α_p, and (b) secondary detuning degree α_s versus xy-misalignment.

the two loosely magnetic couplers are similar to x-misalignment and air gap misalignment, while the cross-coupling M_{psf} is gradually increased with the misalignment, which may affect the detuning degree of the system.

Similarly, the detuning degree of the secondary and primary sides can be shown in Figs. 14 and 15. For the x-misalignment, the primary detuning degree α_p and the secondary detuning degree α_s of the proposed method are located in [0, 5.33] and [0, 0.05], while that of the traditional method is [0, 32.66] and [0, −0.09], respectively. Although the detuning degree α_p and

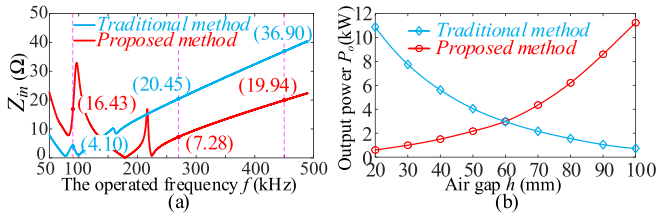

Fig. 16. Profile of (a) input impedance versus the frequency and (b) output power versus the air gap.

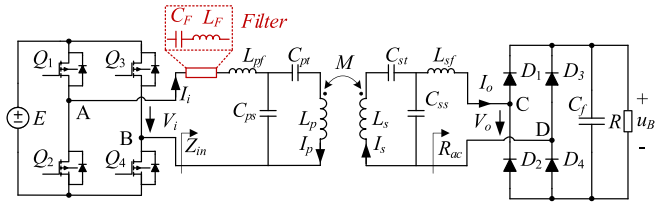

Fig. 17. Double-sided *LCC*-compensated topology with *LC* filter.

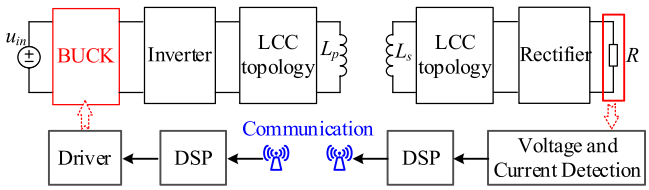

Fig. 18. Control scheme.

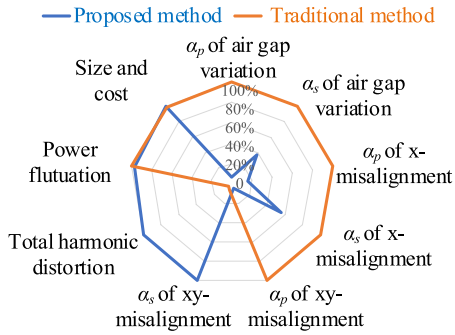

Fig. 19. Performance comparison.

α_s of the primary side and the secondary side for the proposed method is slightly higher than the traditional method when air gap is low (30 mm), the overall α_p and α_s of the proposed method are significantly superior to that of the traditional method when air gap and x-misalignment vary in [30, 90 mm] and [0, 150 mm]. When there is xy-misalignment, the variation trends of the primary detuning degree α_p is similar to the x-misalignment and air gap misalignment, but the secondary detuning degree α_s of the proposed method gets worse with the effect of the cross-coupling M_{psf}, the maximum value of α_s and P_o are 1.2 when the xy-misalignment is 141.42 mm and the air gap is 30 mm.

Besides, the harmonics are introduced to the system due to the square voltage waveforms present in the rectifier input and inverter output. Unlike the traditional design method, the resonant relationship between L_{pf} (L_{sf}) and C_{ps} (C_{ss}) is lost in the proposed method. This nonresonance may lead to the filter property of the proposed method being inferior to that of the traditional method. Using (6), the input impedance of the system with different frequencies can be displayed in Fig. 16(a). The graph indicates that the fundamental harmonic (90 kHz) input impedance of the proposed method is greater than that of the traditional method. However, the input impedance of the third and fifth harmonics is lower, suggesting the presence of a significant amount of high-order harmonics in the proposed method [37]. Thus, a series resonant filter consisting of capacitor C_F and inductor L_F should be added to attenuate these harmonics, as seen in Fig. 17. Moreover, the relationship between C_F and L_F should satisfy $\omega^2 L_F C_F = 1$ according to [15].

Furthermore, the transfer power can be calculated in Fig. 16(b) using (20). The two methods exhibit opposite power variation trends during the predetermined range of air gap variation. Due to the loss of the resonant relationship between L_{pf} (L_{sf}) and C_{ps} (C_{ss}), the transfer power of the proposed method no longer decreases with a rise (or increases with a decline) in the air gap (coupling), unlike in the traditional resonant double-sided *LCC*-compensated topology. However, it is more similar to the traditional resonant SS topology, where the transfer power increases with the declining air gap and decreases with the rise in the coupling, as indicated by (32). In order to maintain constant output power, a buck circuit is employed on the primary side [23]. By communicating the output voltage u_B and current i_B collected from the load, the controller adjusts the duty ratio acting on the buck circuit to achieve a relatively constant power transfer. The corresponding control scheme is provided in Fig. 18.

In order to comprehensively evaluate the proposed method, the analysis results can be concluded in Fig. 19. The maximum values are selected for readability in each comparison aspect, and the data are scaled equally. It can be seen that the proposed method and the traditional method have similar power fluctuation. Although the total harmonic distortion is inferior to the traditional method, a filter can suppress the system harmonic by slightly compromising the cost [49]. Regarding the detuning degree, the proposed method is significantly lower than the traditional method for air gap variation. For the x-misalignment, although the detuning degree of the proposed method is slightly inferior to the conventional method when the air gap is low (30 mm), the overall detuning degree of the proposed method is still superior to that of the traditional method. For the xy-misalignment, the secondary detuning degree of the proposed method is higher, but the primary detuning can be alleviated. To sum up, this article is more suitable for applications where the lateral displacement can be negligible, but the air gap variation (vertical displacement) is significant, such as the AGV [9], and so on.

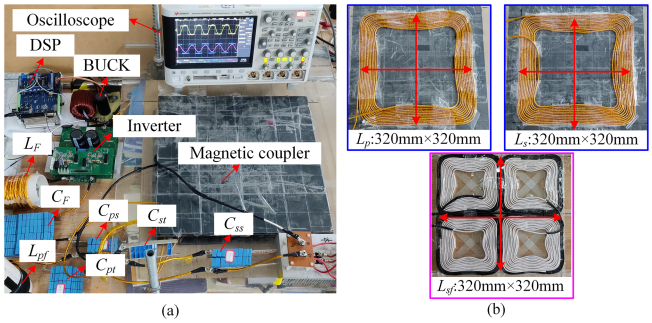

Fig. 20. Experimental prototype. (a) Overall setup. (b) Coils structure.

TABLE III
DEVICE'S MODELS

Device	Model
DC power source	Chroma 62150H-600
MOSFETs	C2M0040120D
Litz wire	AWG38 × 4.2 mm
Ferrite core	PC40
Rectifier diode	DSEI2×61−06C
Electronic load	ITECH IT8816B

IV. EXPERIMENTAL RESULTS AND DISSUSION

A. Experiment Results

To validate the effectiveness of the proposed method, a 1-kW experimental prototype is constructed and displayed in Fig. 20. Two sets of parameters were determined for each method and subsequently measured. These parameters, along with the corresponding devices, are listed in Tables I–III. The experimental prototype was tested under diverse conditions using these components to assess the effectiveness and performance of the proposed method.

The waveforms for the air gap of 30, 60, and 90 mm are depicted in Fig. 21. When the system operates with an air gap of 30 mm, the input impedance angle θ and the phase angle ϕ between I_p and I_s are closed to 0° and 90°, respectively, i.e., the resonance conditions of the secondary and primary side are achieved both the proposed method and the traditional method. When the air gap increases to 60 mm, the variation of LCT parameters results in increased θ and ϕ values for both methods. The proposed method resulted in θ and ϕ values of 18.4° and 92.3°, respectively, whereas the traditional method produced values of 52.6° and 86.4°, respectively. When the air gap increases to 90 mm, the traditional method is associated with θ and ϕ values of 77.8° and 85.1°, respectively, while the proposed method returns to a state of approximate resonance. Besides, the experimental waveforms of MOSFET Q_1 for the proposed method are given in Fig. 22 with different air gaps. As evident from the figure, the soft turn-ON for the semiconductor switches is achieved by operating with the minimum, median, and maximum air gap, which indicates that the ZVS can be fulfilled within the air gap range [30–90 mm]. Fig. 23 presents the measurements of the input impedance angle θ and the phase angle ϕ between I_p and I_s. The overall detuning degree shows that the traditional method experienced a change in θ and ϕ from 1.7° and 90.1° to 77.8° and 85.1°, respectively, indicating inferior performance compared to the proposed method's ([7.3°, 18.3°] and [89.4°, 92.3°]) outcomes. Additionally, the results in Fig. 23 show slight differences when compared to the calculated values in Fig. 12. The differences are primarily attributable to the interference of the harmonic and resistance in each reactive element. Despite these differences, the results remain acceptable.

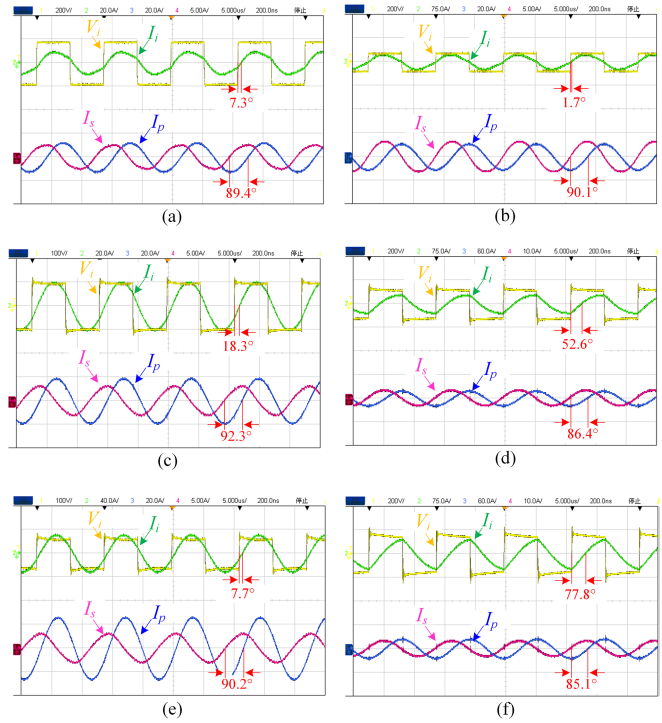

Fig. 21. Measured waveforms of V_i, I_i, I_p, and I_s, where (a), (c), and (e) are that of the proposed method while (b), (d), and (f) are that of the traditional method when the air gap is, respectively, 30, 60, and 90 mm.

The output power is measured in Fig. 24(a). The regulation of the buck circuit ensures that output power fluctuation is less than 1%, and that the output power is almost constant at 1 kW for both proposed and traditional methods. Moreover, the overall system efficiency is given in Fig. 24(b). It can be seen that the efficiency of the proposed method is always higher than the traditional method. There are two main reasons as follows:

1) When the air gap is small, both systems operate under resonant conditions. However, the traditional method's buck circuit needs to use a larger duty cycle to maintain constant output power, as shown in Figs. 16(b) and 21(a) and (b), leading to more power loss.
2) As the air gap increases, the resonant conditions of the proposed method can be adaptively restored, leading to the reduction of power loss caused by the reactive current. The efficiency of the proposed method decreases from 92.63% to 74.81% with an increase in the air gap, whereas that of the traditional method varies between 66.65% and 88.58%. The maximum improvement in efficiency is 8.16% when the air gap is 90 mm. The results verify the effectiveness of the proposed method.

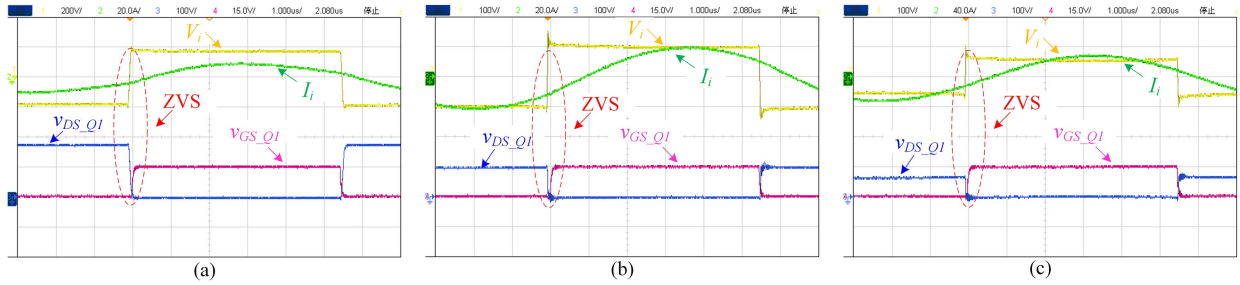

Fig. 22. Waveforms of MOSFET Q_1 when the air gap is (a) 30 mm, (b) 60 mm, and (c) 90 mm, where v_{GS_Q1} and v_{DS_Q1} are the gate drive signal and voltage of MOSFET Q_1, respectively.

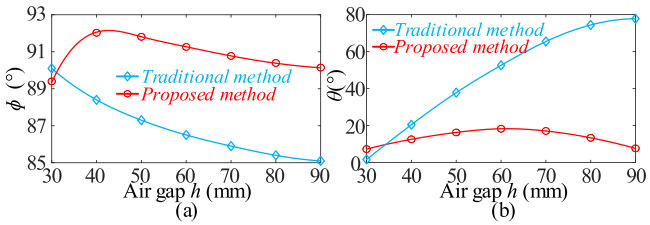

Fig. 23. Measured results of (a) phase angle ϕ between I_p and I_s, and (b) input impedance angle θ.

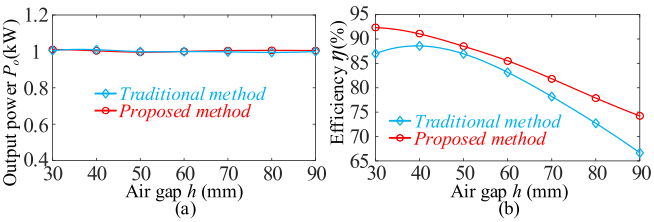

Fig. 24. Measured (a) output power and (b) efficiency versus air gap h.

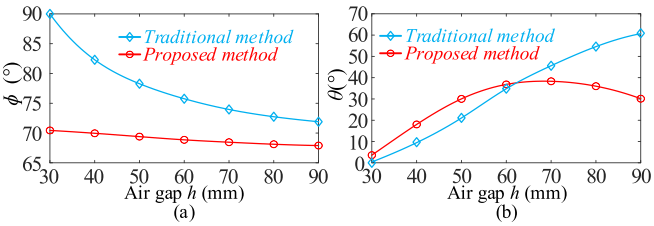

Fig. 25. Measured results of (a) phase angle ϕ between I_p and I_s, and (b) input impedance angle θ when $R = 80\ \Omega$.

Changes in load cause deviation in the detuning degree α_s and α_p from the original near-resonance cases according to (4), (7), (19), and (22). θ and ϕ with 80 Ω are illustrated in Fig. 25. With an increase in air gap from 30 to 90 mm, the θ and ϕ values for the proposed method with 80 Ω vary from 3.6° and 70.44° to 38.2° and 67.9°, resulting in inferior primary and secondary detuning degrees than the rated load case (40 Ω). For the traditional method with 80 Ω, θ and ϕ increase from 0.9° and 89.4 to 60.7° and 71.9° with an increasing air gap, indicating a less severe case for the secondary detuning degree than that of the proposed

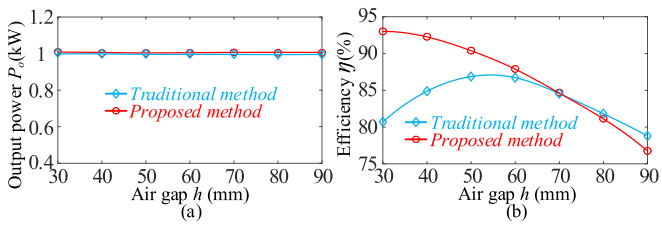

Fig. 26. Measured (a) output power and (b) efficiency versus air gap h when $R = 80\ \Omega$.

method with 80 Ω. However, the primary detuning degree is still serious. The output power and efficiency are measured in Fig. 26. Similarly, at smaller values of h, a larger modulation range is required to maintain constant output power, leading to lower efficiency for the traditional method than the proposed method. The maximum difference in efficiency is 12.26% at $h = 30$ mm. The efficiency of the proposed method decreases gradually as the air gap increases due to the synergistic effect of circuit detuning, decreased coupling, and buck circuit regulation. When the air gap is operated within [70, 90 mm], the efficiency of the proposed method is no longer greater than that of the traditional method, with the maximum reduction in efficiency being 3.03% at $h = 90$ mm. Nevertheless, in terms of average efficiency, the proposed method (84.27%) is superior to the traditional method (82.84%) when the air gap is within the required range [30, 90 mm].

B. Comparison and Discussion

A detailed comparison table is given in Table IV to show the superiority of the proposed method. Compared to the traditional impedance adjustment method (capacitor matrix [12], variable capacitor [13], [14], [15], and variable inductor [16], [17], [19]), the extra switch components and dc source can be saved. Although the extra *LC* filter is required in the proposed method, the constant output regulation, primary tuning, and secondary tuning can be simultaneously achieved compared with the frequency control methods [20], [21], [22]. For [23], the dc–dc control method is more suitable for the multicoils system, and it is hard to achieve tuning of the two-coils system. Compared to the active control methods of rectifier [24], [25], [26], this article does not require an extra transformer and measurement coil. Although

TABLE IV
COMPARISON OF TUNING METHODS

Ref.	System structure	Tuning strategy	Additional components	Control difficulty	Power level	Maximum efficiency	Constant output	Primary tuning	Secondary tuning
[13]	Double-SPP (two-coils)	Capacitor matrix	$M \times N$ capacitors and switches, an LC filter	Complex	1 W	90%	Yes	Yes	No
[14]	Z-S (two-coils)	Variable capacitor	A variable switched capacitor	Medium	3.47 kW	96.88%	Yes	Yes	No
[15]	LCC-S (two-coils)	Variable capacitor	A variable switched capacitor	Easy	54 W	76.6%	No	Yes	No
[16]	LCC-S (two-coils)	Variable capacitor	Two variable switched capacitors, an LC filter	Complex	700 W	86.9%	Yes	Yes	Yes
[17]	Multicoils	Variable inductor	A magnetic saturation and an extra dc source	Easy	Null	Null	No	Yes	No
[18]	S-S (two-coils)	Variable inductor	Two magnetic saturation inductors and an extra dc source	Easy	Null	Null	No	No	Yes
[20]	LCC-S (two-coils)	Variable inductor	A transformer, a rectifier, and a BUCK circuit	Medium	400 W	91%	Yes	No	Yes
[21]	S-S (two-coils)	Frequency control	/	Easy	Null	Null	No	Yes	No
[22]	Two-coils and four-coils	Frequency control	/	Easy	Null	Null	No	Yes	No
[23]	Multicoils	Frequency control	/	Easy	25 W	Null	No	Yes	No
[24]	Multicoils	DC–DC control	/	Medium	80 W	92.9%	Yes	Yes	No
[25]	S-S (two-coils)	Active control of rectifier	A transformer, a measurement coil	Complex	800 W	91.7%	Yes	No	Yes
[26]	S-S (two-coils)	Frequency control, active control of rectifier	A transformer, a measurement coil	Complex	80 W	82%	No	Yes	Yes
[27]	LCC-S (two-coils)	Active control of rectifier	An extra rectifier, an extra dc source	Medium	3.6 W	30.3%	Yes	No	Yes
[29]	S-S (two-coils)	Active control of rectifier	/	Easy	145 W	88.43%	No	No	Yes
This work	Double-LCC (two-coils)	Integrated inductor	A filter	Easy	1 kW	92.67%	Yes	Yes	Yes

TABLE V
COMPARISON BETWEEN THIS WORK AND THE EXISTING WORKS USING DOUBLE-*LCC* TOPOLOGY

Ref.	System structure	Design condition			Operating frequency	Power level	Maximum efficiency
		Self-inductance of the primary coil	Self-inductance of the secondary coil	Mutual inductance			
[33]	Double-LCC	33.78 uH (fixed)	32.64 uH (fixed)	6.54 uH (fixed)	85 kHz	2 kW	92.14%
[35]	Double-LCC	120 uH (fixed)	120 uH (fixed)	18 uH (fixed)	81.5 kHz, 90 kHz	3.3 kW	92.6%
[36]	Double-LCC	16.18 uH (fixed)	15.52 uH (fixed)	5.82 uH (fixed)	206.6 kHz, 259.9 kHz	250 W	93%
[37]	Double-LCC	218.3 uH (fixed)	218.3 uH (fixed)	57.3 uH (fixed)	68 kHz, 79.1 kHz	6.6 kW	96.1%
[38]	Double-LCL	97.7 uH (fixed)	97.7 uH (fixed)	22.77 uH (fixed)	85 kHz	200 W	90.2%
[39]	Double-LCL	360 uH (fixed)	240 uH (fixed)	23.5–50 uH (variable)	85 kHz	3.3 kW	95.2%
[40]	Double-LCC	35 uH (fixed)	36 uH (fixed)	4.37–6.11 uH (variable)	85 kHz	1 kW	91.6%
[41]	Double-LCC	40 uH (fixed)	40 uH (fixed)	6.56 uH (Fixed)	85 kHz	6.6 kW	92.4%
This work	Double-LCC	130.35–155.00 μH (variable)	131.17–156.16 μH (variable)	40.8–95.99 μH (variable)	90 kHz	1 kW	92.63%

some parameter identification methods [27], [28] have been proposed to eliminate extra components, it can be challenging in situations where there is an air gap variation because some parameters (including the value of the compensated capacitor and self-inductance) are required to obtain in advance. Admittedly, because the proposed method just employs inherent characteristics of the IPT system to alleviate the detuning of the system, the tuning accuracy may be inferior to the methods [12], [13], [14], [15], [16], [17], [18], [19], [20], [21], [22], [23], [24], [25], [26], [27], [28]. However, the proposed method is superior in terms of cost, complexity, and whole-tuning capability.

Furthermore, many outstanding works using double-sided *LCC*-compensated topology are proposed to improve the system performance. To further clarify the unique contributions of the proposed method, comparison results are given in Table V. It can be seen that most of the existing works are aimed at the application with fixed LCT parameters (self-inductance and mutual inductance) [32], [33], [34], [35], [36], [40]. Although the methods reported in [38] and [39] can be applied in misalignment cases, the LCT's self-inductances must be fixed or slightly varied. Once the self-inductances of coils are changed with displacement, the system performance is degraded due to the nonresonance of the system. Differing from the existing works [32], [33], [34], [35], [36], [37], [38], [39], [40], this article is to improve the system performance in the cases of LCT parameters variation versus air gap. The core idea is to replace the inductor on the secondary side with an integrated inductor to form a compact magnetic coupler structure. This integrated inductor changes its value with variations in the air gap to neutralize the detuned part caused by variations in LCT parameters. Therefore, the main contributions and implementation methods between this work and the existing works [32], [33], [34], [35], [36], [37], [38], [39], [40] are quite different.

V. Conclusion

In summary, the efficiency of the IPT system is significantly affected by detuning on the secondary and primary sides. The traditional approach struggles to maintain resonant conditions due to LCT parameter variations when there are significant air gap alterations. To address this, we propose a double-sided *LCC*-compensated topology with an integrated inductor in this article. The variation of the integrated inductor can be employed to neutralize the detuning degree caused by the LCT parameter variations in relation to the air gap, enabling the system to operate in an approximately resonant state. Moreover, we propose a parameter design method to maintain system detuning within a specific range of variation. In the experiments, the proposed method consistently kept input impedance angles and phase angles between the primary and secondary coil currents within [7.3°, 18.3°] and [89.4°, 92.3°], respectively, as the air gap varied between 30 and 90 mm. Conversely, the traditional method maintains angles in wider intervals of [1.7°, 77.8°] and [90.1°, 85.1°]. These results suggest that the proposed method can efficiently alleviate the system's detuning degree. Additionally, the proposed IPT system efficiency ranges from 74.81% to 92.63%, marking a 8.16% maximum efficiency improvement compared to the traditional method. These results endorse the robust performance of the proposed method. Moreover, while the system tuning performance of the proposed method suffered deterioration caused by load variation, this issue will be addressed in the future. Nonetheless, our proposed method's average system efficiency still outperforms the traditional method when the load changes.

References

[1] S. R. Khan, S. K. Pavuluri, G. Cummins, and M. P. Y. Desmulliez, "Wireless power transfer techniques for implantable medical devices: A review," *Sensors*, vol. 20, no. 12, Jun. 2020, Art. no. 3487.

[2] R. Saha, B. Roy Joy, and S. A. Mirbozorgi, "Wireless power transmission with uniform power delivery in the 3D space of the human body using resonators in parallel," in *Proc. 43rd Annu. Int. Conf. IEEE Eng. Med. Biol. Soc.*, 2021, pp. 7268–7271.

[3] S. A. Mirbozorgi, P. Yeon, and M. Ghovanloo, "Robust wireless power transmission to mm-sized free-floating distributed implants," *IEEE Trans. Biomed. Circuits Syst.*, vol. 11, no. 3, pp. 692–702, Jun. 2017.

[4] S. A. Mirbozorgi, E. Maghsoudloo, H. Bahrami, M. Sawan, and B. Gosselin, "Multi-resonator arrays for smart wireless power distribution: Comparison with experimental assessment," *Inst. Eng. Technol. Power Electron.*, vol. 13, no. 18, pp. 4183–4193, Feb. 2021.

[5] P. Shi, Y. Cao, H. Zhao, R. Gao, and S. Liu, "Parallel strips coupled split ring resonators for a desktop wireless charging system overcoming irregular route restrictions," *J. Magnetism Magn. Mater.*, vol. 563, Oct. 2022, Art. no. 170005.

[6] Y. Chen et al., "A clamp circuit-based inductive power transfer system with reconfigurable rectifier tolerating extensive coupling variations," *IEEE Trans. Power Electron.*, to be published, doi: 10.1109/TPEL.2023.3303487.

[7] H. Fukuda, N. Kobayashi, K. Shizuno, S. Yoshida, M. Tanomura, and Y. Hama, "New concept of an electromagnetic usage for contactless communication and power transmission in the ocean," in *Proc. IEEE Int. Underwater Technol. Symp.*, 2013, pp. 1–4.

[8] W. Y. Lee et al., "Finite-width magnetic mirror models of mono and dual coils for wireless electric vehicles," *IEEE Trans. Power Electron.*, vol. 28, no. 3, pp. 1413–1428, Mar. 2013.

[9] B. Yang et al., "Analysis and design of a T/S compensated IPT system for AGV maintaining stable output current versus air gap and load variations," *IEEE Trans. Power Electron.*, vol. 37, no. 5, pp. 6217–6228, May 2022.

[10] S. Li, G. Zhang, X. Lei, X. Yu, H. Qian, and Y. Xu, "Trajectory tracking control of a unicycle-type mobile robot with a new planning algorithm," in *Proc. IEEE Int. Conf. Robot. Biomimetics*, 2017, pp. 780–786.

[11] J. S. Choi, S. Y. Jeong, B. G. Choi, S.-T. Ryu, C. T. Rim, and Y.-S. Kim, "Air-gap-insensitive IPT pad with ferromagnetic and conductive plates," *IEEE Trans. Power Electron.*, vol. 35, no. 8, pp. 7863–7872, Aug. 2020.

[12] Y. Lim, H. Tang, S. Lim, and J. Park, "An adaptive impedance-matching network based on a novel capacitor matrix for wireless power transfer," *IEEE Trans. Power Electron.*, vol. 29, no. 8, pp. 4403–4413, Aug. 2014.

[13] Y. Wang et al., "Compact Z-impedance compensation for inductive power transfer and its capacitance tuning method," *IEEE Trans. Ind. Electron.*, vol. 70, no. 4, pp. 3627–3640, Apr. 2023.

[14] D.-H. Kim and D. Ahn, "Self-tuning LCC inverter using PWM-controlled switched capacitor for inductive wireless power transfer," *IEEE Trans. Ind. Electron.*, vol. 66, no. 5, pp. 3983–3992, May 2019.

[15] W. Li, G. Wei, C. Cui, X. Zhang, and Q. Zhang, "A double-side self-tuning LCC/S system using a variable switched capacitor based on parameter recognition," *IEEE Trans. Ind. Electron.*, vol. 68, no. 4, pp. 3069–3078, Apr. 2021.

[16] C. Li et al., "Variable-inductor based tuning method for multiple-relay wireless power transfer system in composite insulator," in *Proc. 5th Asia Energy Elect. Eng. Symp.*, 2023, pp. 390–395.

[17] T. Sasatani, Y. Narusue, Y. Kawahara, and T. Asami, "DC-based impedance tuning method using magnetic saturation for wireless power transfer," in *Proc. IEEE Wireless Power Transfer Conf.*, 2017, pp. 1–4.

[18] Z. Li, H. Liu, Y. Huo, J. He, Y. Tian, and J. Liu, "High-misalignment tolerance wireless charging system for constant power output using dual transmission channels with magnetic flux controlled inductors," *IEEE Trans. Power Electron.*, vol. 37, no. 11, pp. 13930–13945, Nov. 2022.

[19] R. Mai, P. Yue, Y. Liu, Y. Zhang, and Z. He, "A Dynamic tuning method utilizing inductor paralleled with load for inductive power transfer," *IEEE Trans. Power Electron.*, vol. 33, no. 12, pp. 10924–10934, Dec. 2018.

[20] D.-W. Seo and J.-H. Lee, "Frequency-tuning method using the reflection coefficient in a wireless power transfer system," *IEEE Microw. Wireless Compon. Lett.*, vol. 27, no. 11, pp. 959–961, Nov. 2017.

[21] R. Huang and B. Zhang, "Frequency, impedance characteristics and HF Converters of two-coil and four-coil wireless power transfer," *IEEE J. Emerg. Sel. Topics Power Electron.*, vol. 3, no. 1, pp. 177–183, Mar. 2015.

[22] X. Hou, Y. Su, Z. Zuo, X. Dai, and Y. Fei, "A novel analysis method based on quadratic eigenvalue problem for multirelay magnetic coupling wireless power transfer," *IEEE Trans. Power Electron.*, vol. 36, no. 9, pp. 9907–9917, Sep. 2021.

[23] J. Jiang, X. Dai, and A. P. Hu, "A dynamic tuning method for ZPA frequency operation of MEU-WPT system by DC input voltages regulation," *IEEE Trans. Power Electron.*, vol. 37, no. 9, pp. 11369–11381, Sep. 2022.

[24] R. Mai, Y. Liu, Y. Li, P. Yue, G. Cao, and Z. He, "An active-rectifier-based maximum efficiency tracking method using an additional measurement coil for wireless power transfer," *IEEE Trans. Power Electron.*, vol. 33, no. 1, pp. 716–728, Jan. 2018.
[25] K. Song et al., "An impedance decoupling-based tuning scheme for wireless power transfer system under dual-side capacitance drift," *IEEE Trans. Power Electron.*, vol. 36, no. 7, pp. 7526–7536, Jul. 2021.
[26] K. Matsuura, D. Kobuchi, Y. Narusue, and H. Morikawa, "Communication-less receiver-side resonant frequency tuning for magnetically coupled wireless power transfer systems," *IEEE Access*, vol. 11, pp. 23544–23556, 2023.
[27] Y. Yang, S. C. Tan, and S. Y. R. Hui, "Front-end parameter monitoring method based on two-layer adaptive differential evolution for SS-compensated wireless power transfer systems," *IEEE Trans. Ind. Inform.*, vol. 15, no. 11, pp. 6101–6113, Nov. 2019.
[28] R. Dai, R. Mai, and W. Zhou, "A pulse density modulation based receiver reactance identification method for wireless power transfer system," *IEEE Trans. Power Electron.*, vol. 37, no. 9, pp. 11394–11405, Sep. 2022.
[29] Y. Chen et al., "Reconfigurable topology for IPT system maintaining stable transmission power over large coupling variation," *IEEE Trans. Power Electron.*, vol. 35, no. 5, pp. 4915–4924, May 2020.
[30] K. N. Mude and K. Aditya, "Comprehensive review and analysis of two-element resonant compensation topologies for wireless inductive power transfer systems," *Chin. J. Elect. Eng.*, vol. 5, no. 2, pp. 14–31, Jun. 2019.
[31] X. Wang, J. Xu, M. Leng, H. Ma, and S. He, "A hybrid control strategy of LCC-S compensated WPT system for wide output voltage and ZVS range with minimized reactive current," *IEEE Trans. Ind. Electron.*, vol. 68, no. 9, pp. 7908–7920, Sep. 2021.
[32] Y. Chen et al., "A parameter tuning method for a double-sided LCC compensated IPT system with constant-voltage output and efficiency optimization," *IEEE Trans. Power Electron.*, vol. 38, no. 3, pp. 4124–4139, Mar. 2023.
[33] S. Li, W. Li, J. Deng, T. D. Nguyen, and C. Mi, "A double-sided LCC compensation network and its tuning method for wireless power transfer," *IEEE Trans. Veh. Technol.*, vol. 64, no. 6, pp. 2261–2273, Jun. 2015.
[34] J. Lu, G. Zhu, D. Lin, S. C. Wong, and J. Jiang, "Load-independent voltage and current transfer characteristics of high-order resonant network in IPT system," *IEEE J. Emerg. Sel. Topics Power Electron.*, vol. 7, no. 1, pp. 422–436, Mar. 2019.
[35] X. Qu, H. Chu, S. C. Wong, and C. K. Tse, "An IPT battery charger with near unity power factor and load-independent constant output combating design constraints of input voltage and transformer parameters," *IEEE Trans. Power Electron.*, vol. 34, no. 8, pp. 7719–7727, Aug. 2019.
[36] V. B. Vu, D. H. Tran, and W. J. Choi, "Implementation of the constant current and constant voltage charge of inductive power transfer systems with the double-sided LCC compensation topology for electric vehicle battery charge applications," *IEEE Trans. Power Electron.*, vol. 33, no. 9, pp. 7398–7410, Sep. 2018.
[37] Y. Yao, Y. Wang, X. Liu, F. Lin, and D. Xu, "A novel parameter tuning method for a double-sided LCL compensated WPT system with better comprehensive performance," *IEEE Trans. Power Electron.*, vol. 33, no. 10, pp. 8525–8536, Oct. 2018.
[38] F. Wang, W. Zhang, L. Ye, J. Guo, K. Liu, and H. T. Do, "A design method to implement ZVS for electric vehicle wireless charging system with double-side LCC compensation," *IEEE J. Emerg. Sel. Topics Power Electron.*, vol. 9, no. 3, pp. 3791–3801, Jun. 2021.
[39] V.-T. Nguyen, V.-B. Vu, G. Gohil, and B. Fahimi, "Coil-to-coil efficiency optimization of double-sided LCC topology for electric vehicle inductive chargers," *IEEE Trans. Ind. Electron.*, vol. 69, no. 11, pp. 11242–11252, Nov. 2022.
[40] Y. Chen, H. Zhang, C.-S. Shin, C.-H. Jo, S.-J. Park, and D.-H. Kim, "An efficiency optimization-based asymmetric tuning method of double-sided LCC compensated WPT system for electric vehicles," *IEEE Trans. Power Electron.*, vol. 35, no. 11, pp. 11475–11487, Nov. 2020.
[41] B. Yang et al., "A clamped IPT system with adaptive mode switching against large coupling variations," *IEEE Trans. Power Electron.*, vol. 38, no. 9, pp. 11694–11704, Sep. 2023.
[42] Y. Chen, S. He, B. Yang, S. Chen, Z. He, and R. Mai, "Reconfigurable rectifier-based detuned series-series compensated IPT system for anti-misalignment and efficiency improvement," *IEEE Trans. Power Electron.*, vol. 38, no. 2, pp. 2720–2729, Feb. 2023.
[43] X. Qu, Y. Yao, D. Wang, S.-C. Wong, and C. K. Tse, "A family of hybrid IPT topologies with near load-independent output and high tolerance to pad misalignment," *IEEE Trans. Power Electron.*, vol. 35, no. 7, pp. 6867–6877, Jul. 2020.
[44] H. Feng, T. Cai, S. Duan, X. Zhang, H. Hu, and J. Niu, "A Dual-side-detuned series–Series compensated resonant converter for wide charging region in a wireless power transfer system," *IEEE Trans. Ind. Electron.*, vol. 65, no. 3, pp. 2177–2188, Mar. 2018.
[45] A. Ahmad, M. S. Alam, and A. A. S. Mohamed, "Design and interoperability analysis of quadruple pad structure for electric vehicle wireless charging application," *IEEE Trans. Transp. Electrific.*, vol. 5, no. 4, pp. 934–945, Dec. 2019.
[46] Y. Chen et al., "A hybrid inductive power transfer system with misalignment tolerance using quadruple-D quadrature pads," *IEEE Trans. Power Electron.*, vol. 35, no. 6, pp. 6039–6049, Jun. 2020.
[47] M. Wu et al., "A compact coupler with integrated multiple decoupled coils for wireless power transfer system and its anti-misalignment control," *IEEE Trans. Power Electron.*, vol. 37, no. 10, pp. 12814–12827, Oct. 2022.
[48] S. Chen, Y. Chen, N. A. Dung, R. Mai, and Y. Tang, "A compact wireless charger design with decoupled quadruple-D inductor for LCC-series topologies," in *Proc. IEEE 4th Int. Future Energy Electron. Conf.*, 2019, pp. 1–7.
[49] C. Xia, R. Chen, Y. Liu, L. Liu, and G. Chen, "Inhibition of current harmonics in LCL/LCC wireless power transfer system," in *Proc. IEEE PELS Workshop Emerg. Technol.: Wireless Power Transfer*, 2017, pp. 1–6.

Bin Yang (Student Member, IEEE) received the B.S. degree in electrical engineering and automation from the School of Electrical and Automation Engineering, East China Jiaotong University, Nanchang, China, in 2017. He is currently working toward the Ph.D. degree in electrical engineering with Southwest Jiaotong University, Chengdu, China.

He is currently a Visiting Ph.D. Student with the Department of Energy, Aalborg University, Aalborg, Denmark. His research interests include wireless power transfer, especially on misalignment tolerance improvement.

Yiming Zhang received the B.Sc. degree in electrical engineering and automation from the School of Electrical Engineering, East China Jiaotong University, Nanchang, China, in 2021. He is currently working toward the M.Sc. degree in electrical engineering with the School of Electrical Engineering, Southwest Jiaotong University, Chengdu, China.

His research interest includes wireless power transfer.

Chenyan Zhu received the B.Sc. degree in electrical engineering and automation, in 2018, from the School of Electrical Engineering, Southwest Jiaotong University, Chengdu, China, where he is currently working toward the Ph.D. degree in electrical engineering.

His research interest includes wireless power transfer.

Subham Sahoo (Senior Member, IEEE) received the B.Tech. degree in electrical and electronics engineering from the VSSUT, Burla, India, in 2014, and the Ph.D. degree in electrical engineering from the Indian Institute of Technology, New Delhi, India, in 2018.

He is currently an Assistant Professor with the Department of Energy, Aalborg University (AAU), Aalborg, Denmark, where he is also the Vice-Leader of the research group on Reliability of Power Electronic Converters (ReliaPEC) with the AAU Energy. His research interests include control, optimization, cybersecurity, and stability of power electronic dominated grids, application of artificial intelligence, and machine learning in power systems.

Dr. Sahoo is a recipient of the Indian National Academy of Engineering Innovative Students Project Award for the best Ph.D. thesis across all the institutes in India for the year 2019. He is selected into EU–US National Academy of Engineering Frontier of Engineering Class of 2021. He was also a Distinguished Reviewer for IEEE TRANSACTIONS ON SMART GRID, in 2020. He is currently the Vice-Chair of IEEE PELS Technical Committee 10 on Design Methodologies. He is an Associate Editor for IEEE TRANSACTIONS ON TRANSPORTATION ELECTRIFICATION.

Yang Chen (Member, IEEE) received the B.Sc. degree in electrical engineering and automation and the Ph.D. degree in electrical engineering from the Southwest Jiaotong University, Chengdu, China, in 2015 and 2020, respectively.

From 2018 to 2019, he was a Visiting Scholar founded by the China Scholarship Council with the Future Energy Electronics Center, Virginia Tech, Blacksburg, VA, USA. From 2020 to 2023, he was a Postdoctoral Researcher with the Southwest Jiaotong University, Chengdu, China, where he is currently an Associate Researcher. His research interest includes wireless power transfer.

Ruikun Mai (Senior Member, IEEE) received the B.Sc. and Ph.D. degrees in electrical engineering from the School of Electrical Engineering, Southwest Jiaotong University, Chengdu, China, in 2004 and 2010, respectively.

He is currently a Professor with the School of Electrical Engineering, Southwest Jiaotong University, Chengdu, China. His research interests include wireless power transfer and its application in railway systems, and power system stability and control.

Zhengyou He (Senior Member, IEEE) received the B.Sc. and M.Sc. degrees in computational mechanics from the Chongqing University, Chongqing, China, in 1992 and 1995, respectively, and the Ph.D. degree in electrical engineering from Southwest Jiaotong University, Chengdu, China, in 2001.

He is currently a Professor with the School of Electrical Engineering, Southwest Jiaotong University. His research interests include signal process and information theory applied to electrical power system, and application of wavelet transforms in power system.

Frede Blaabjerg (Fellow, IEEE) is honoris causa at University Politehnica Timisoara, Romania, and the Tallinn Technical University, Tallinn, Estonia. He received the Ph.D. degree in electrical engineering from Aalborg University, Aalborg, Denmark, in 1995.

He was with the ABB-Scandia, Randers, Denmark, from 1987 to 1988. He became an Assistant Professor in 1992, an Associate Professor in 1996, and a Full Professor of power electronics and drives in 1998. In 2017, he became a Villum Investigator. He has authored/coauthored more than 600 journal papers in the fields of power electronics and its applications. He has coauthored four monographs and is an editor of ten books in power electronics and its applications. His research interests include power electronics and its applications, such as in wind turbines, PV systems, reliability, harmonics, and adjustable speed drives.

Dr. Blaabjerg was the recipient of the 32 IEEE Prize Paper Awards, the IEEE PELS Distinguished Service Award in 2009, the EPE–PEMC Council Award in 2010, the IEEE William E. Newell Power Electronics Award 2014, the Villum Kann Rasmussen Research Award 2014, the Global Energy uPrize in 2019, and the 2020 IEEE Edison Medal. He was the Editor-in-Chief of IEEE TRANSACTIONS ON POWER ELECTRONICS from 2006 to 2012. He was a Distinguished Lecturer for IEEE POWER ELECTRONICS SOCIETY from 2005 to 2007 and for IEEE INDUSTRY APPLICATIONS SOCIETY from 2010 to 2011 as well as 2017 to 2018. In 2019–2020, he served a President of IEEE POWER ELECTRONICS SOCIETY. He is Vice-President of the Danish Academy of Technical Sciences too. He is nominated in 2014–2019 by the Thomson Reuters to be between the most 250 cited researchers in Engineering in the world.